



**Spatially adaptive estimation of multi-layer soil temperature at a daily time-step
across China during 2010-2020**

Xuetong Wang^{1, 2}, Liang He^{3, *}, Peng Li^{1, 2}, Jiageng Ma⁴, Yu Shi⁵, Qi Tian^{1, 2}, Gang
Zhao^{2, 6}, Jianqiang He⁷, Hao Feng², Hao Shi^{8, 9, *}, Qiang Yu^{2, *}

¹ College of Natural Resources and Environment, Northwest A&F University, Yangling
712100, China

² State Key Laboratory of Soil and Water Conservation and Desertification Control,
Northwest A&F University, Yangling 712100, China

³ National Meteorological Center, Beijing, 100081, China

⁴ Key Laboratory of Ecosystem Network Observation and Modeling, Institute of
Geographic Sciences and Natural Resources Research, Chinese Academy of Sciences,
Beijing 100101, PR China

⁵ Institute of Carbon Neutrality, Sino-French Institute for Earth System Science, College
of Urban and Environmental Sciences, Peking University, Beijing 100871, China

⁶ College of Soil and Water Conservation Science and Engineering, Northwest A&F
University, Yangling, Shaanxi, 712100, China

⁷ Key Laboratory for Agricultural Soil and Water Engineering in Arid Area of Ministry
of Education, Northwest A&F University, Yangling 712100, China

⁸ State Key Laboratory for Ecological Security of Regions and Cities, Research Center
for Eco-Environmental Sciences, Chinese Academy of Sciences, Beijing, 100085,
China

⁹ College of Resources and Environment, University of Chinese Academy of Sciences,
Beijing, 100049, China

Correspondence:

Liang He (heliang_hello@163.com)

Hao Shi (haoshi@rcees.ac.cn)

Qiang Yu (yuq@nwafu.edu.cn)



Abstract

Soil temperature (T_s) is critical in regulating agricultural production, ecosystem functions, hydrological cycling and climate dynamics. However, the inherent spatial and temporal heterogeneity of soil thermal regimes constitutes a persistent challenge in

5 obtaining high-resolution, continuous gridded T_s datasets along vertical profiles. To address this issue, we propose a spatially adaptive layer-cascading Extreme Gradient Boosting (XGBoost) algorithm to generate daily multi-layer T_s data (0, 5, 10, 15, 20, and 40 cm) at a spatial resolution of 1 km in China from 2010 to 2020. The methodology dynamically partitions non-uniformly distributed measuring sites (2,093 sites across the

10 country) to quadtrees and incorporates thermal coupling effects propagated between neighbor soil layers. Multi-source data, including satellite retrievals of land surface temperature and vegetation index, and ERA5 reanalysis climate variables were used as inputs. Independent tests demonstrated high robustness and accuracy of our model, with depth-specific values of coefficients of determination (R^2) being 0.94~0.98 and root

15 mean square errors (RMSE) values ranging 1.75~2.21K. It is noted the model's performance was lower in summers and winters than in springs and autumns. Compared to existing global or regional T_s products, the dataset developed here is characterized by its fine spatio-temporal patterns and high reliability, enabling it to provide supports for precision agriculture, ecosystem modeling and understanding climate-land feedback.

20 Free access to the dataset can be found at <https://doi.org/10.11888/Terre.tpd.302333> (Wang et al., 2025).

Key words: Soil temperature, spatially adaptive, machine learning, multi-source data



30 1. Introduction

Soil temperature (T_s) is a critical driver of ecosystem dynamics, influencing nearly all physical, chemical, and biological processes (Bayatvarkeshi et al., 2021; Xu et al., 2023; Liu et al., 2025). T_s plays a pivotal role in land-atmosphere exchanges. By controlling the partitioning of net radiation into sensible and latent heat fluxes, T_s directly shapes atmospheric boundary layer circulation, with cascading effects on regional climate patterns (Mahanama et al., 2008; L. Chen et al., 2021). T_s also drives soil freeze-thaw cycles, which are critical for hydrological processes in cold regions. Permafrost thaw alters subsurface water storage, runoff dynamics and groundwater recharge, with implications for both local and basin-scale hydrology (Zhang et al., 2005; Shati et al., 2018). In addition, it governs the rates of soil microbial activities, nutrient cycling, and organic matter decomposition, with direct implications for carbon dynamics. For instance, T_s modulates microbial respiration, thereby regulating the release of organic carbon into the atmosphere as CO_2 that is central to global carbon cycling (Yang et al., 2011). Given its multifaceted influences on carbon cycling, climate feedbacks and hydrological systems, accurate T_s estimation is indispensable for advancing ecosystem monitoring, refining climate models, and developing effective strategies to mitigate and adapt to climate change.

T_s exhibits high heterogeneity at large spatial scales due to varying driving factors. Solar radiation changes its radiation intensity by adjusting the incident angle and sunshine duration, thus affecting the heating effects on surface soils (Wang and Dickinson, 2013). Additionally, diurnal variations of air temperature cause periodic changes in surface temperature, while the amplitude is often closely related to the local climate and topography. Furthermore, surface covers (e.g., vegetation and snow) significantly impact T_s (Xu et al., 2020; Mortier et al., 2024). Vegetation canopies effectively intercept and scatter solar radiation, while root systems modulate soil moisture distribution, thereby stabilizing deeper soil temperatures (Li et al., 2024). Snow cover, characterized by high albedo, reflects substantial solar radiation and acts as an effective insulator, mitigating cold air penetration and maintaining warmer soil



temperatures during winter months (Myers-Smith et al., 2015). Moreover, thermal
60 conductivity and heat capacity are critical parameters controlling vertical heat transfer
in soils. Sandy soils have higher porosity and lower water retention, resulting in lower
heat capacity and higher thermal conductivity, thus responding rapidly to temperature
changes. In contrast, clay soils have lower porosity and stronger water retention, leading
to higher heat capacity and significant thermal stability, characterized by delayed
65 responses to temperature variations (Ochsner et al., 2001; Zhao et al., 2022).
Understanding these mechanisms is essential for developing refined vertical T_s
distribution models and improving the accuracy of T_s estimation.

Given these complex processes, accurately estimating T_s across different depths is
challenging. Quite a few models have been proposed for T_s estimation. These models
70 can be generally classified into physical, statistical or empirical, and machine learning
(ML) types (Li et al., 2024; Farhangmehr et al., 2025). Physical models, derived from
fundamental heat conduction laws and energy balance equations, provide explicit
mechanistic interpretations but suffer from computational complexity and heavy
reliance on multi-domain input parameters, which range from soil properties to climatic
75 variables (Gao et al., 2008; Hu et al., 2016; Badache et al., 2016). Statistical or empirical
models, such as autoregressive integrated moving average and regression methods
(Xing et al., 2018), are usually limited to localized, small-sample applications. Data-
driven machine learning techniques demonstrate a superior ability to capture nonlinear
relationships and thus usually can obtain high prediction accuracy. For instance, at site
80 scale, Feng et al. (2019) estimated multi-layer T_s at half-hourly resolutions using
Extreme Learning Machine, with a RMSE ranging from 2.26~2.95 K. Li et al., (2022)
implemented an attention-aware long short-term memory (LSTM) model for predicting
next-day T_s and the model obtained a RMSE of 0.74~2.53 K. At the regional scale, Xu
et al. (2023) integrated satellite remote sensing with a deep belief network model to
85 reconstruct continuous T_s profiles (at depths of 5–40 cm) across the Qinghai-Tibetan
Plateau (QTP), obtaining $R^2 > 0.836$ and $MAE < 2.152$ °C. Similarly, Farhangmehr et
al. (2025) developed a hybrid convolutional neural network-LSTM (CNN-LSTM)



architecture for predicting T_s across North American climatic zones at 0-7 cm depths, with R^2 ranging from 0.93 to 0.99.

90 Although significant advances have been made in estimating T_s , large-scale T_s prediction continues to confront critical challenges, sourcing from environmental complexity and methodological limitations. First, T_s exhibits considerable spatial heterogeneity driven by regional disparities in topography, soil composition, vegetation density, and microclimate (Bayatvarkeshi et al., 2021). These factors create
95 nonstationary relationships between T_s and explanatory variables (e.g., air temperature, soil moisture), necessitating regionally tailored modeling approaches. Second, data scarcity and uneven spatial distribution of site measurements introduce further complexity. Aggregating sparse, unevenly distributed measurements into a single model often leads to overfitting: high accuracy on training data but poor generalization to
100 underrepresented regions or previously unseen data (Li et al., 2024). Ultimately, developing models that reconcile scalability (for large spatial scales) with localized precision (to capture site-specific interactions) remains an unresolved priority, underscoring the persistent challenge of balancing universal applicability with spatially adaptive fidelity in T_s prediction methodology.

105 In this study, we propose a spatial scale-adaptive methodology based on quadtrees for multi-layer T_s estimation. The objectives are to: (1) develop a novel modeling framework by integrating multi-source data, including in-situ observations, remote sensing products, meteorological variables, and auxiliary environmental data; (2) generate a multi-layer T_s dataset at a daily time-step and one kilometer resolution in
110 China from 2010-2020; and (3) assess the accuracy of the dataset through independent validation and benchmarking against widely used T_s products. The proposed methodology could explicitly address the scaling challenges induced by spatial heterogeneity and uneven data distribution. The generated products would provide a robust foundation for high-resolution environmental modeling, precision agriculture
115 and climate impact assessments.



2. Materials and methods

2.1 In-situ T_s observations

In this study, in-situ T_s observations were sourced from the China Meteorological Administration, encompassing daily mean T_s data collected from 2,093 stations across the period 2010–2020. These stations recorded T_s at six standard soil depths: 0, 5, 10, 15, 20, and 40 cm. The observation network spans a wide range of climatic zones— from cold and temperate to subtropical and tropical, and includes diverse land-use and ecosystem types, such as forests, grasslands, croplands, and barren lands. However, the spatial distribution of stations is notably uneven. High station density is observed in northeastern China, the central and eastern plains, and the southern hilly regions, whereas station coverage is sparse in the arid and semi-arid regions of northwestern China and on the QTP. Figure.1 illustrates the spatial configuration of the dataset: gray dots represent samples used for model training, while red dots denote those reserved for model testing. Details regarding the dataset partitioning strategy are provided in Section 2.3.3.

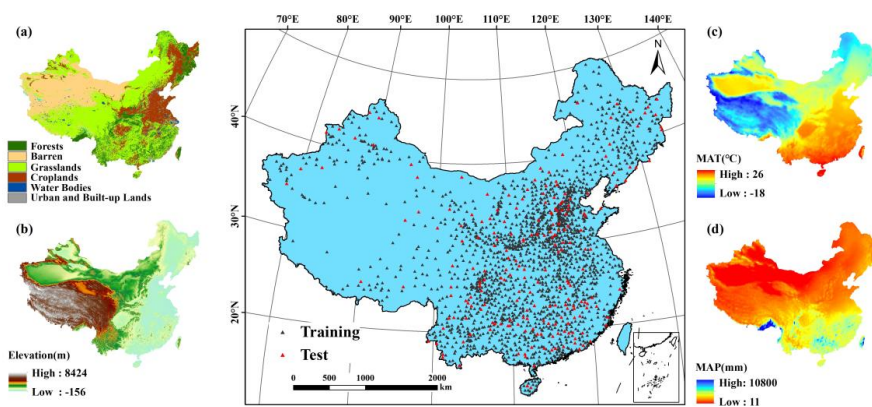


Figure 1. Spatial distribution of in-situ T_s sites at different depths across China and the corresponding environmental variables. This figure presents the spatial distribution of 2,093 in-situ T_s sites across China, with samples divided into the training set (gray) and the test set (red). The environmental variables corresponding to these sites include (a) land cover types (forests, barren land, grasslands, croplands, water bodies, and urban areas), (b) elevation (ranging from -156 m to 8424 m), (c) mean annual temperature (MAT, ranging from -18°C to 26°C), and (d) mean annual precipitation (MAP, ranging from 11 mm to 10,800 mm).



2.2 Predictor variables

To construct a robust multi-layer T_s estimation model, we selected a comprehensive suite of predictor variables, integrating remote sensing products, meteorological factors, and auxiliary environmental data. Meteorological variables, especially air temperature and precipitation, have been consistently recognized in previous studies as primary determinants of T_s variability (Bond-Lamberty et al., 2005; Nahvi et al., 2016). Among these, air temperature has been widely regarded as the most influential variable due to its strong linear relationship with T_s (Khosravi et al., 2023). In addition, solar radiation was included, given its significant role in regulating the surface energy balance through its influence on net radiation, latent heat flux, and ground heat flux, all of which directly affect T_s dynamics.

Thermal infrared remote sensing data also exhibit a high correlation with near-surface T_s . Integrating thermal remote sensing products and energy balance-based models offers an effective means of estimating T_s with high spatial and temporal continuity. This strategy has been validated by numerous studies (Huang et al., 2020; Xu et al., 2023). Surface land cover further modulates T_s by altering surface albedo, regulating evapotranspiration (ET), and influencing energy partitioning processes. Accordingly, the enhanced vegetation index (EVI), derived from satellite observations, was incorporated as a proxy for vegetation density and type (Bright et al., 2017; N. Li et al., 2024). To capture the influence of underlying surface characteristics on T_s , topographic variables such as elevation and slope were included, along with soil texture data across various depths. These features collectively reflect the heterogeneous physical and thermal properties of the soil, contributing to spatial variations in heat conduction and storage capacity. A full list of the predictor variables used in the model is summarized in Table 1.

Table 1. Details of the predictor variables for training the model.

Type	Data	Variable	Spatial resolution	Temporal resolution	Reference
Remotely sensed product	MOD09GA	EVI	500 m×500 m	Daily	Huete et al., 2002
	MOD11A1	LST_Day	1 km×1 km	Daily	



	MOD11A1	LST_Night	1 km×1 km	Daily	
Climate data	ERA5-Land	Temperature_2m			Muñoz-Sabater et al., 2021
		Solar_radiation	9 km×9 km	Daily	
		Precipitation			
		Wind_10m			
Supplementary data	USGS_STRM	Elevation	30 m		Liu et al., 2022
		Slope	30 m		
	Soil Texture	Sand, Silt, Clay			
		Depth: 0-5, 5-15, 15-30, 30-60cm	250 m×250 m		
		In-situ measurements	Soil temperature at 0, 5, 10, 15, 20, and 40 cm	-	

2.2.1 Remote sensing data

170 The MOD11A1 LST product, at a daily time-step and a spatial resolution of 1 km, was utilized. It includes both daytime (LST_{day}) and nighttime (LST_{night}) temperatures at 10:30 AM and 10:30 PM, respectively, along with quality assessment information (Wan and Dozier, 1996). To enhance the estimation of daily mean T_s , the average of LST_{day} and LST_{night} values was calculated and used in the analysis.

175 EVI from 2010 to 2020 were selected as predictor of T_s . The MODIS Surface Reflectance Product (MOD09GA), derived from MODIS Level-1B data, provides daily surface reflectance of seven bands at 500 m × 500 m resolution. The EVI is defined by Huete et al., (2002), and the retrieval equation is as follows:

$$EVI = G \times \frac{(\rho_{SR_b1} - \rho_{SR_b2})}{(\rho_{SR_b1} + C_1 \times \rho_{SR_b2} - C_2 \times \rho_{SR_b3} + L)} \quad (1)$$

180 where $G = 2.5$, $C_1 = 6$, $C_2 = 7.5$, $L = 1$. The remote sensing reflectance variables SR_b1 (620-670nm), SR_b2 (841-876nm) and SR_b3 (459-479 nm) of MOD09GA data represents red, near-infrared and blue bands. The coefficients 2.5 and 1 represent the gain and canopy background, respectively (Huete et al., 2002). The atmospheric influence on the red band is corrected using the blue band and the coefficients 6 and 185 7.5, respectively.

Subsequently, cloud contamination caused partial spatial absences in the daily LST



and EVI. To address this issue, we applied a temporal and spatial linear interpolation algorithm, which utilizes time-series data from adjacent days and spatial information from neighboring pixels to fill the current missing values, thereby generating a time-
190 continuous and spatially complete image series. This approach follows the methods described in Chen et al., (2017) and Cao et al., (2018), with modifications to better suit our dataset. Then, the Savitzky-Golay (S-G) filter was used to smooth the interpolated data, resulting in continuous surface temperature and vegetation index data with high temporal and spatial resolution (Kong et al., 2019; Y. Chen et al., 2021). All data
195 preprocessing, including image filtering and interpolation, was conducted within the Google Earth Engine (GEE) platform.

2.2.2 Climate data

The ERA5-Land is the fifth-generation reanalysis dataset produced by the
200 European Centre for Medium-Range Weather Forecasts (ECMWF). It assimilates multi-source data, including weather station measurements, numerical weather predictions, and satellite observations, into dynamic models to generate reanalysis data (Muñoz-Sabater et al., 2021). It provides high-quality environmental variables related to water and energy fluxes between the land surface and atmosphere, with continuous
205 coverage from 1981 to the present. ERA5-Land offers a spatial resolution of 0.1° (~ 9 km at the equator) and an hourly temporal resolution, making it well-suited for modeling near-surface processes. In this study, we extracted daily mean values of key climate variables, including 2-meter air temperature (Temperature_2m), surface solar radiation, total precipitation, and 10-meter wind speed (wind_speed_10m), from the
210 ERA5-Land Daily dataset. All variables were accessed and processed using the GEE platform.

2.2.3 Auxiliary data

Topographic and soil-related variables were incorporated as auxiliary predictors to
215 improve the accuracy of T_s estimation. Elevation and slope were derived from the



Shuttle Radar Topography Mission (SRTM) digital elevation model (Farr et al., 2007), specifically using the Version 3 (SRTM Plus) product with a spatial resolution of 1 arc second (~30 m). Soil texture plays a critical role in determining T_s through its influence on thermal conductivity, which is affected by physical properties such as particle size distribution, porosity, bulk density, and moisture retention capacity. In this study, we represented soil texture using the relative proportions of clay (fine), silt (medium), and sand (coarse) particles. To capture vertical variability in soil properties, we employed the China Soil Information Grid dataset developed by Liu et al. (2022), which provides gridded estimates of soil composition at four depth intervals: 0–5 cm, 5–15 cm, 15–30 cm, and 30–60 cm. The dataset offers a spatial resolution of 1 km and is suitable for high-resolution, profile-based soil modeling.

2.3 Methods

The spatial adaptive modeling framework consists of three modules as shown in Fig. 3. Module I is for data collection and preprocessing, which mainly involves in-situ observations, remote sensing, meteorological and supplementary data. Module II is spatial adaptive modeling, which mainly includes the construction of rotated quadtrees and local modeling based on XGBoost. Finally, module III is the layer-to-layer reconstruction of daily 1km resolution multi-layer (0, 5, 10, 15, 20, and 40 cm) T_s datasets in China from 2010 to 2020.

2.3.1. Feature selection

To mitigate multicollinearity among predictor variables, we calculated the Variance Inflation Factor (VIF) for all candidate features (Akinwande et al., 2015). As shown in Fig. S1, both the daily mean LST (LST_mean) and air temperature exhibited high collinearity, with VIF values exceeding 10. Although LST_mean offers higher spatial resolution (1 km) compared to air temperature (9 km), it is crucial to recognize that these two variables are physically distinct. Their differences become particularly pronounced in complex ecosystems such as forests, where canopy structure and



245 biological processes significantly influence thermal dynamics (Liu et al., 2025). Given
these considerations, both LST_mean and air temperature were retained for the
estimation of T_s at the 0 cm depth, as they offer complementary information. Following
feature selection, all retained variables were resampled to a common spatial resolution
of 1 km using bilinear interpolation to ensure consistency in subsequent modeling steps.

250

2.3.2. Spatial adaptive partition of site measurements

A quadtree is a hierarchical spatial data structure that recursively subdivides a two-
dimensional space into four quadrants, enabling efficient spatial indexing and localized
data organization. In this study, we adopted a rotated quadtree-based spatial partitioning
255 strategy to facilitate region-specific T_s modeling. The procedure comprises the
following steps:

(1) Initialization of Minimum Units

The entire spatial domain was first divided into uniform, minimum-sized units
(leaf nodes), each representing a fundamental spatial element. These units may contain
260 zero or more in-situ observations. This initial step provides the base resolution for
subsequent hierarchical construction. The structure and principle of quadtree spatial
indexing are illustrated in Fig. S2.

(2) Hierarchical Merging

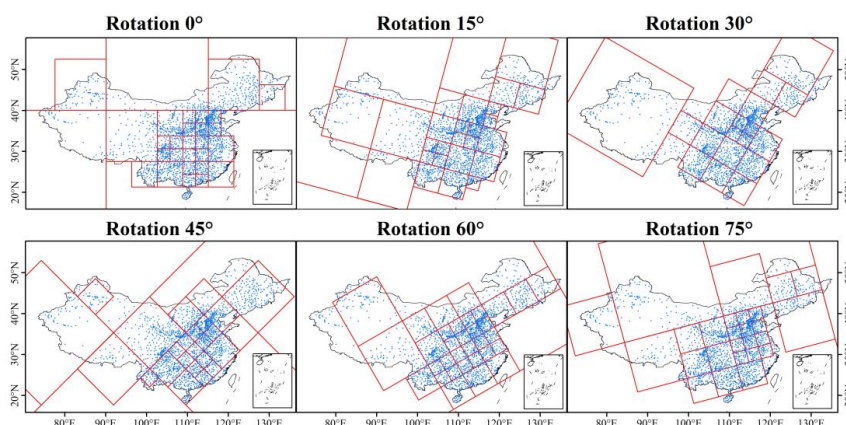
Beginning with the leaf nodes, neighboring quadrants (i.e., groups of four adjacent
265 nodes) were recursively merged into parent nodes if they satisfied a specified threshold:
each sub-node contained fewer than 30 observational sites. This criterion ensures a
balance between regional modeling precision and sample size sufficiency. The merging
process continued upward through the hierarchy until no further aggregation met the
threshold. The resulting partitions define spatially adaptive subregions, each of which
270 is assigned a localized T_s prediction model.

(3) Rotation at different angles

To address potential edge effects introduced by static grid boundaries, we
implemented a rotated quadtree partitioning strategy. The quadtree structure was rotated



at six angles (0° , 15° , 30° , 45° , 60° , and 75°), producing distinct sets of spatial partitions
275 for each orientation (Fig. 2). Independent models were trained for each rotated
configuration, and the final T_s estimates were obtained by averaging the outputs from
all six models. This rotational ensemble approach enhances spatial continuity and
reduces boundary artifacts in the final predictions.



280 **Figure 2.** multi-angle adaptive quadtree partitioning of site observations (0° , 15° , 30° ,
 45° , 60° , 75°)

2.3.3. Machine learning algorithm

We selected the XGBoost (Extreme Gradient Boosting) algorithm for T_s estimation
due to its proven accuracy, computational efficiency, and scalability for large-scale
285 regression tasks. Introduced by Chen and Guestrin, (2016), XGBoost constructs an
ensemble of regression trees in a sequential manner, where each new tree is trained to
correct the residuals of the preceding ones. This iterative boosting process continues
until convergence criteria are met, and the final prediction is obtained by aggregating
the outputs of all trees. Compared to other machine learning algorithms such as support
290 vector machines, random forests, and neural networks, XGBoost offers optimized
performance through parallel computing, efficient memory usage, and a second-order
gradient descent optimization strategy that accelerates training. Its robustness and
predictive power have been widely demonstrated in geoscience and remote sensing
applications, including land surface temperature reconstruction (Li et al., 2024) and



295 multi-layer soil moisture estimation (Karthikeyan and Mishra, 2021).

As shown in Fig. 3, the observational dataset was stratified into training (70%), validation (20%), and test (10%) subsets through random sampling. A separate XGBoost model was constructed for each spatial grid using the Python XGBoost package (Chen and Guestrin, 2016). To prevent overfitting, model hyperparameters
300 were carefully tuned. Specifically, we optimized key parameters including the number of trees (`n_estimators`), maximum tree depth (`max_depth`), and learning rate (`eta`). GridSearchCV was applied to conduct an exhaustive search over the hyperparameter space defined in Table S1. Five-fold cross-validation was used to evaluate model generalizability and identify the optimal hyperparameter combinations for each local
305 model.

A layer-wise prediction strategy was adopted to estimate T_s along the soil profile. For the surface layer (0 cm), predictors included air temperature and daily mean LST. For subsurface layers, these two variables were replaced by the T_s estimate from the immediately preceding layer, allowing the model to account for vertical temperature
310 conduction processes and improving the continuity of layer-wise T_s estimation.

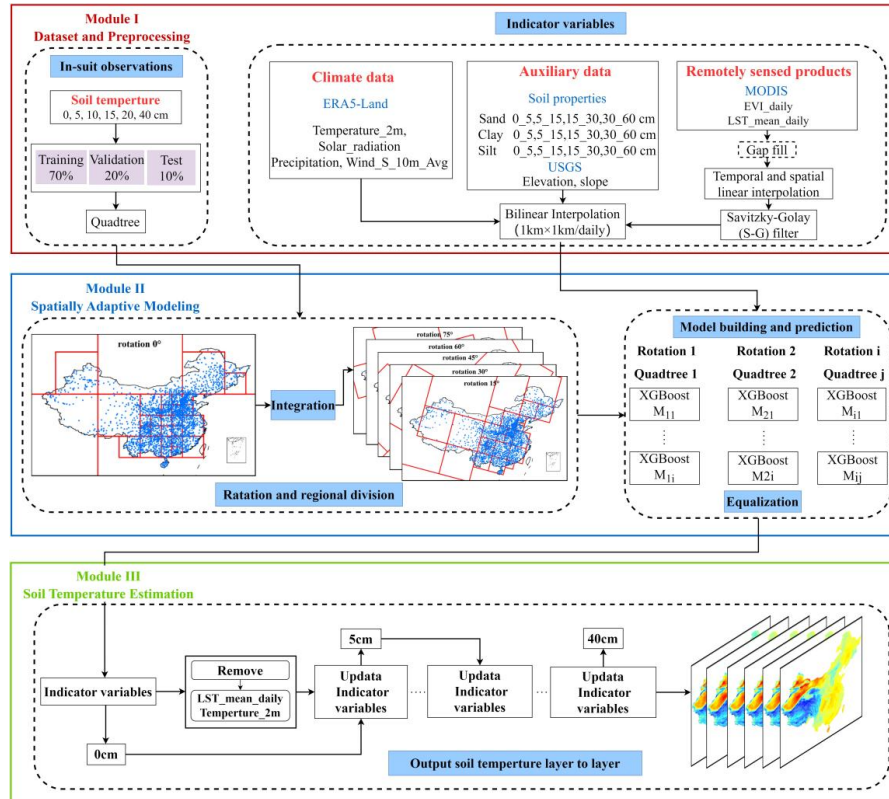


Figure 3. Workflow of the proposed method to obtain multi-layer T_s over the China.

315 2.3.4. Model evaluation metrics

The modeling performance and quality of the predicted T_s were evaluated in terms of RMSE, Mean Absolute Error (MAE), R^2 , and Bias. RMSE and MAE were used to assess the ability to estimate volatility and fluctuation amplitude, respectively. R^2 represented the percentage of variance explained by the ML models. Bias was used to
 320 determine whether the estimations were overestimated or underestimated. These metrics were computed as follows:

$$RMSE = \sqrt{\frac{\sum_{i=1}^N [(x - \bar{X}) - (y - \bar{Y})]^2}{N}} \quad (2)$$

$$MAE = \frac{\sum_{i=1}^N |x_i - y_i|}{2} \quad (3)$$



325

$$\text{Bias} = x_i - y_i \quad (4)$$

$$R^2 = 1 - \frac{\sum_{i=1}^N (y_i - x_i)^2}{N \sum_{i=1}^N (y_i - \bar{Y})^2} \quad (5)$$

where y_i and x_i denoted the in-situ T_s and estimated T_s for all the stations and periods,
330 respectively. \bar{Y} and \bar{X} represented the mean values of the in-situ T_s and estimated T_s ,
respectively.

3. Results

3.1 Model performance across sites

335 Figure 4 illustrates the accuracy performance of all models constructed at various
depths, utilizing different grid configurations and rotation angles, for both the training
and validation sets. The grouped box plots demonstrate that the R^2 values for the
training and validation sets at different depths range from 0.82 to 0.98, and the RMSE
values vary from 0.6 to 2.8 K. Both the training and validation sets exhibit high
340 accuracy with no evident signs of overfitting. A depth-wise comparison shows that
model performance at 0 cm and 40 cm is marginally lower than at other depths.

Additionally, we evaluated the model's performance at different depths using an
independent dataset comprising 210 sampling sites. Final predictions at each site were
obtained by averaging the outputs from six rotations. Figure 5 presents scatter density
345 plots comparing the predicted results with in-situ observations. The results at all depths
are close to the 1:1 reference line. The R^2 values for different depths range from 0.93 to
0.97, and RMSE values between 1.74 and 2.25 K. Although the validation accuracy at
depths of 0 cm and 40 cm is marginally lower than at 5, 10, 15, and 20 cm, the
independent validation results across all depths demonstrate excellent overall
350 performance. Overall, the accuracy validation results from the model's training set,
validation set, and independent sample points indicate that the spatially adaptive model
we developed has robust accuracy and strong generalization capability.

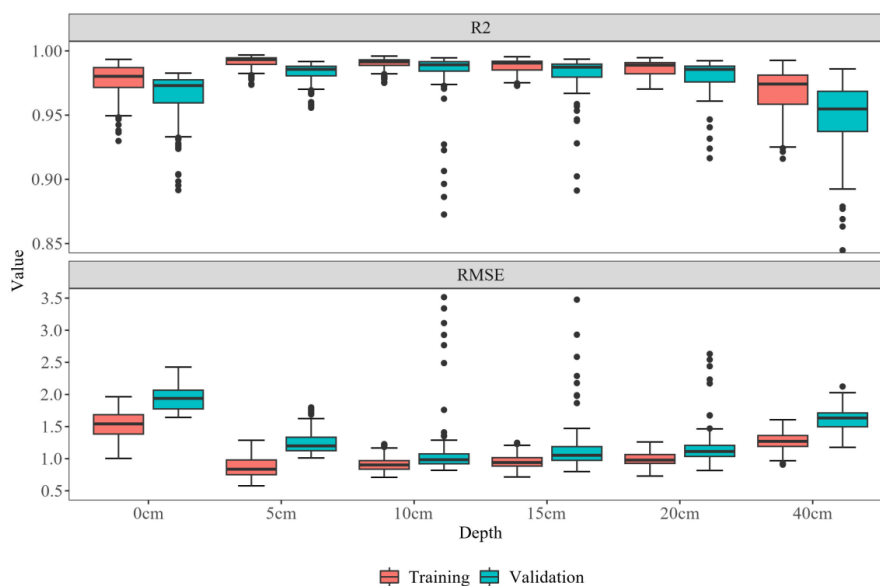


Figure 4. Accuracy performance of model (different rotations and depths) training and validation set

355

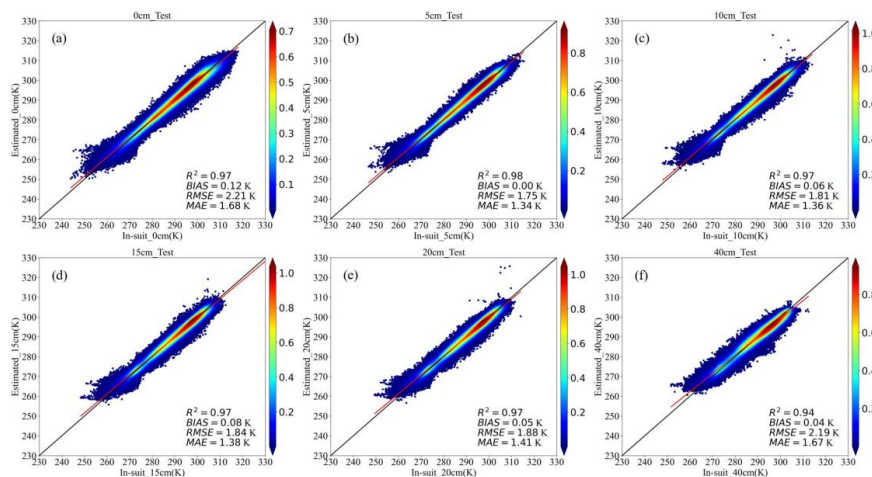


Figure 5. Scatter density plot comparing the accuracy of different depths in the test set

360

3.2 Model performance at individual sites

To evaluate spatial prediction accuracy in the spatial-scale evaluation, R^2 and RMSE were calculated at each station. Model performance was assessed across all soil



depths at the station level. Spatial results show that station-level R^2 values range from
365 0.70 to 1.00, and RMSE values range from 0 to 3 K, indicating acceptable prediction
accuracy across all soil layers. As illustrated in Figures 6 and 7, most stations achieve
 R^2 values above 0.90. Regions with higher prediction accuracy are mainly located in
the northwest, northeast, and central areas, whereas larger errors are concentrated in the
Yunnan–Guizhou Plateau (YGP) and the sparsely monitored QTP. The histogram in Fig.
370 7 further shows that RMSE values for most depths fall between 0.5 and 2.0 K, indicating
generally good predictive performance. Notably, Prediction errors at the surface layer
(0 cm) are notably higher than those at greater depths. In general, error decreases with
increasing depth, although a slight increase is observed at 40 cm, where performance is
slightly poorer than at 5–20 cm.

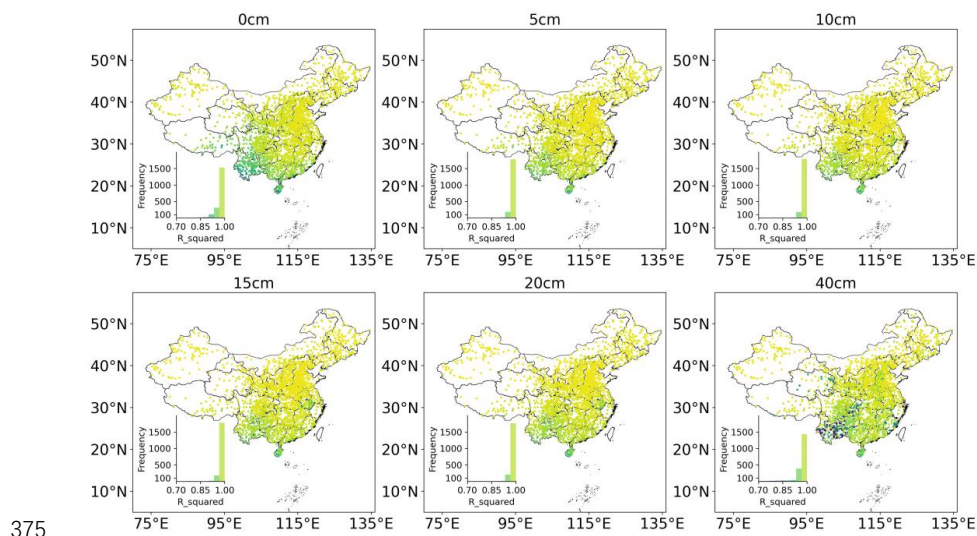
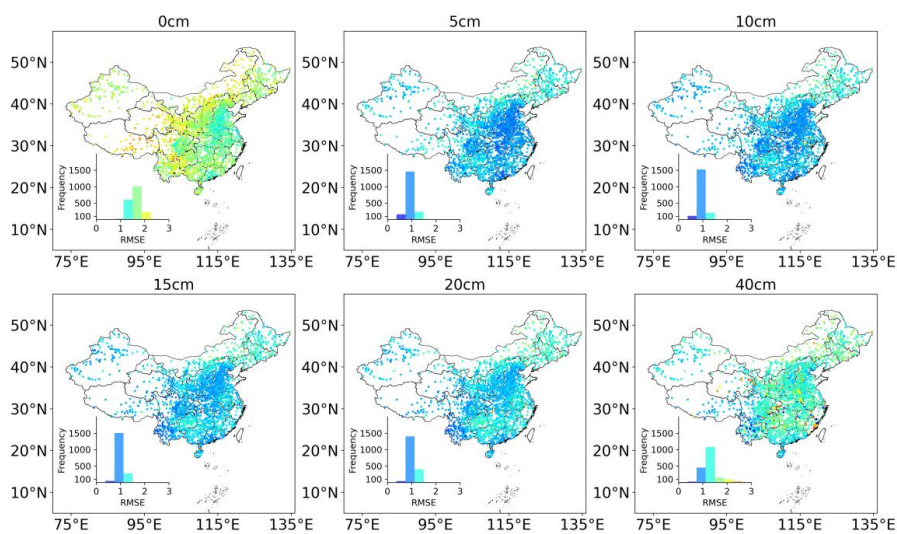


Figure 6. Goodness of R^2 across China estimated during the model testing phase. Performance metrics are calculated between predicted T_s and in-situ T_s data sets.



380

Figure 7. Goodness of RMSE across China estimated during the model testing phase. Performance metrics are calculated between predicted T_s and in-situ T_s data sets.

3.3 Evaluation across land cover types and seasons

385

Figure 8 shows grouped box plots illustrating the prediction performance of T_s across different land cover types (bare land, farmland, forest, grassland) at six depths (0 cm, 5 cm, 10 cm, 15 cm, 20 cm, 40 cm). The evaluation metrics include the R^2 and RMSE. Mean R^2 values across all depths and land cover types range from 0.82 to 0.98, indicating overall high prediction accuracy. Notably, the mean R^2 values consistently exceed 0.96 (indicated by the red dashed line). Among the land cover categories, bare land exhibits the highest R^2 values, followed by farmland, whereas forest and grassland exhibit slightly lower performance. RMSE values vary depending on both soil depth and land cover type, generally ranging from 0.6 to 2.8 K. Bare land displays higher RMSE values, likely due to larger diurnal temperature variations and a relatively small sample size. In contrast, farmland, forest, and grassland show lower and more stable RMSE values. The highest RMSE is observed at the surface layer (0 cm), reflecting the strong sensitivity of shallow soil temperatures to external environmental conditions. RMSE tends to decrease with depth, although a slight increase is noted at 40 cm, where prediction errors are marginally higher than those at 5-20 cm.

390

400

Furthermore, seasonal variations in prediction accuracy are further presented in



Fig. 9. The results demonstrate that the R^2 values in spring (green) and autumn (pink) are significantly higher than those in summer (orange) and winter (blue), particularly at shallow depths (0 cm and 5 cm). This suggests that the model captures T_s variability more effectively during spring and autumn. Seasonal RMSE values range approximately from 0.98 to 1.97 K, with the highest errors occurring at 0 cm depth during summer and winter. These elevated errors are likely attributed to increased surface temperature fluctuations driven by external environmental factors such as solar radiation, which add complexity to the prediction. Overall, RMSE decreases with increasing soil depth across all seasons, indicating improved thermal stability and enhanced prediction accuracy in deeper layers.

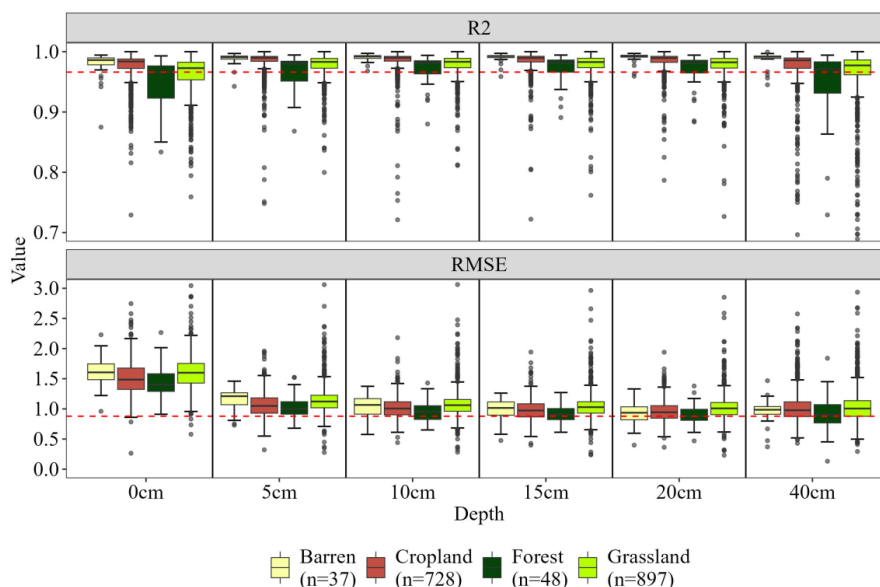
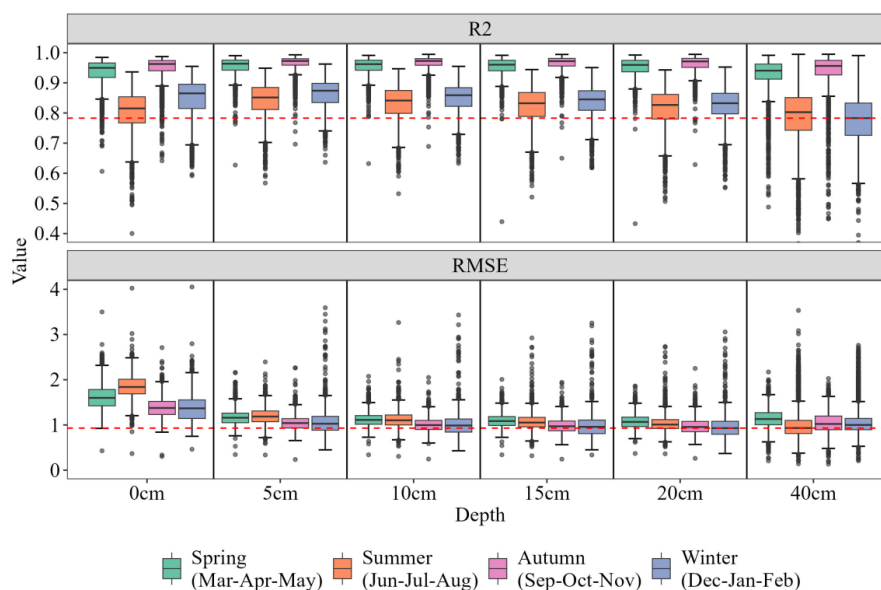


Figure 8. Evaluation of predicted T_s at different depths (i.e., 0, 5, 10, 15, 20, 40cm) across various land use types (i.e., Forest, Grassland, Cropland, Barren)



415

Figure 9. Evaluation of the predicted T_s in different depth (ie.0,5,10,15,20,40 cm) at sites with four seasons (i.e., spring, summer, autumn, winter). Winter is defined as December, January, and February; spring as March, April, and May; summer as June, July, and August; and autumn as September, October, and November.

420

3.4 Comparison with other products

Figure 10 presents a comparative analysis of different T_s products at the surface (0 cm depth), evaluating the spatial characteristics of the model-generated T_s against the ERA5-Land and GLDAS 2.1 products across both national-scale regions (Fig. 10a–c) and zoomed-in local areas (Fig. 10d–f). Compared to the GLDAS 2.1 product (Fig. 11c and 11f), the model generated T_s exhibits significantly finer spatial resolution and a superior ability to capture localized spatial heterogeneity. The GLDAS 2.1 product, characterized by a coarser resolution, inadequately represents local features and exhibits notable limitations, especially in specific regions (Fig. 10f). Conversely, the spatial distribution of our T_s data closely matches that of the ERA5-Land product (Fig. 10b and 10e). Nevertheless, the ERA5-Land product may be constrained by its input resolution, whereas our adaptive modeling approach achieves greater precision in representing fine-scale spatial variability.

430

Scatter density plots in Fig. S3 further indicate that our estimated T_s achieves



435 significantly higher site-level accuracy compared to ERA5-Land and GLDAS 2.1.
Specifically, the R^2 values between in-situ observations and our estimations at depths
of 0, 10, and 40 cm range from 0.94 to 0.97, compared to 0.83–0.89 for ERA5-Land
and 0.83–0.87 for GLDAS 2.1. These results underscore the reliability and enhanced
accuracy of our T_s estimation product at both spatial and site scales, effectively
440 overcoming the limitations associated with GLDAS 2.1 and ERA5-Land products.
These findings highlight the strong potential of the model to accurately capture the
spatial distribution of T_s and enhance regional-scale T_s modeling.

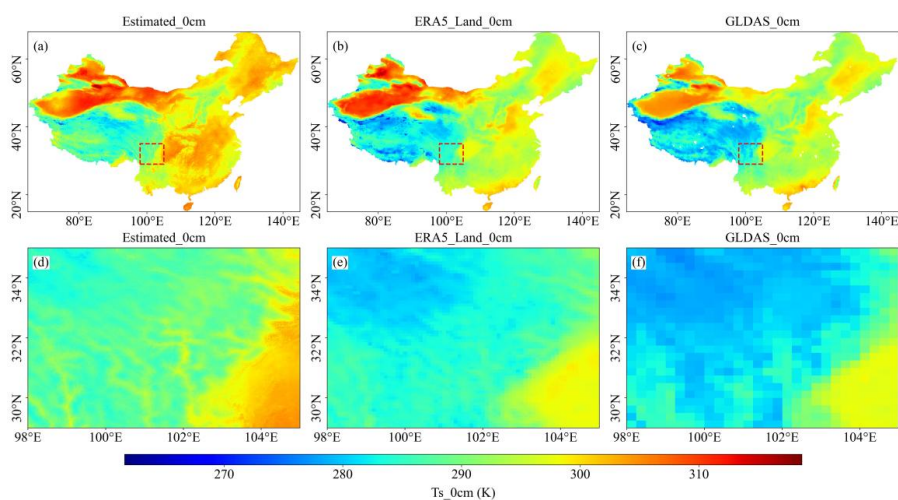


Figure 10. Comparison of different T_s products (e.g., 0 cm)

445

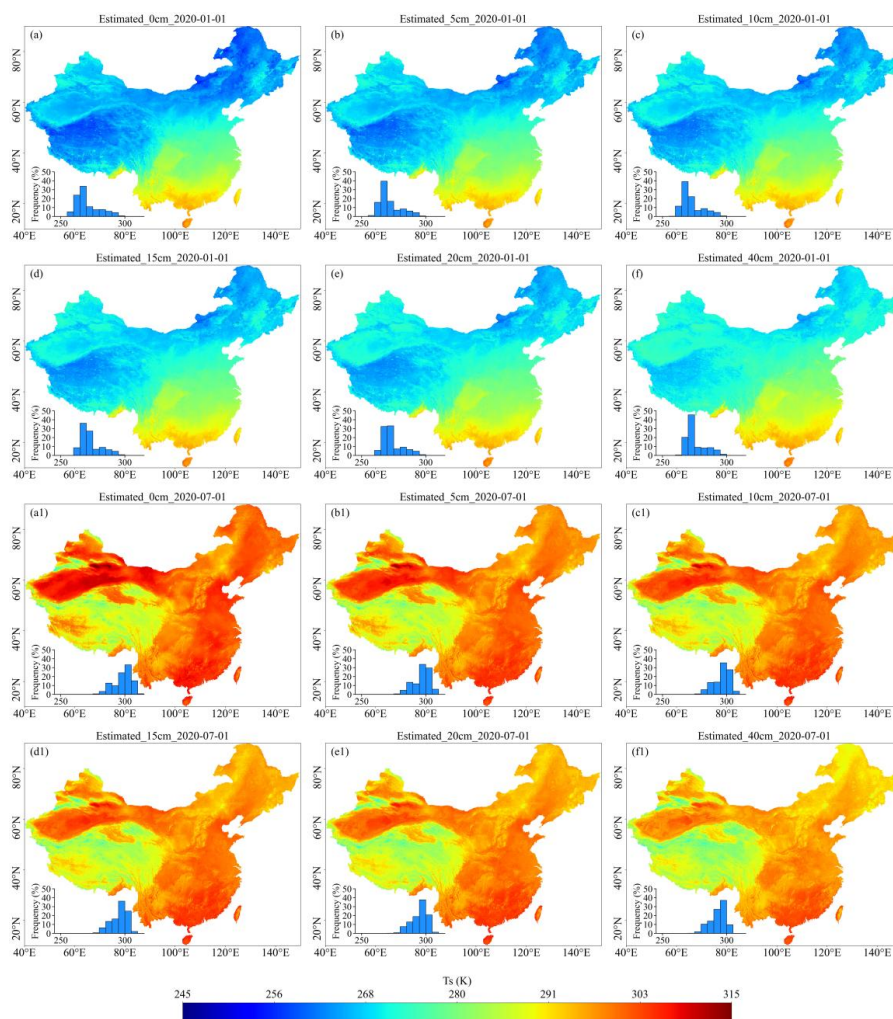
3.5 Spatial and temporal patterns of T_s at varied soil depths across China

To examine seasonal and vertical variations in the spatial distribution of T_s , we
selected two contrasting dates: January 1, 2020 (winter) and July 1, 2020 (summer).
Figure 11 a–f illustrates the spatial distribution and corresponding histograms of T_s
at different depths (0 cm, 5 cm, 10 cm, 15 cm, 20 cm, 40 cm) across China on January 1,
450 2020. The results show that T_s in northern China (particularly in the northeast, northwest,
and the QTP) is generally lower in January, exhibiting distinct cold zones. In contrast,
southern areas exhibit higher T_s values, forming a gradual north-to-south temperature
gradient. Moreover, deeper soil layers (e.g., 40 cm) exhibit higher temperatures than
455 surface layers (0 cm), especially in northeastern China and the QTP, reflecting the



insulating effect of deeper soils during winter.

Figure 11a1–f1 illustrates the spatial distribution and histograms of T_s on July 1, 2020. Compared to January, a significant increase in T_s is observed across China in July, with widespread high-temperature zones in the eastern and southern regions. The increase is particularly pronounced in northern areas, while changes in the south are relatively moderate. In contrast to winter conditions, T_s decreases with increasing soil depth during summer, with surface temperatures (0 cm) exceeding those at 40 cm, indicating the downward heat conduction from the surface. Overall, Comparative analysis of Fig. 11a–f and Fig. 11a1–f1 elucidates both seasonal variation and vertical patterns of T_s : deeper layers (5–40 cm) are warmer than the surface (0 cm) during winter, whereas the surface is warmer in summer. The histogram further illustrates the variation in soil temperature distribution across different depths. The results indicate that temperature fluctuations in deeper soil layers are significantly smaller than those near the surface, reflecting greater thermal stability in the subsurface. These patterns reflect the combined influences of geographic location, topography, and climatic conditions on T_s spatial distribution and vertical dynamics, offering valuable insights into soil thermal behavior.

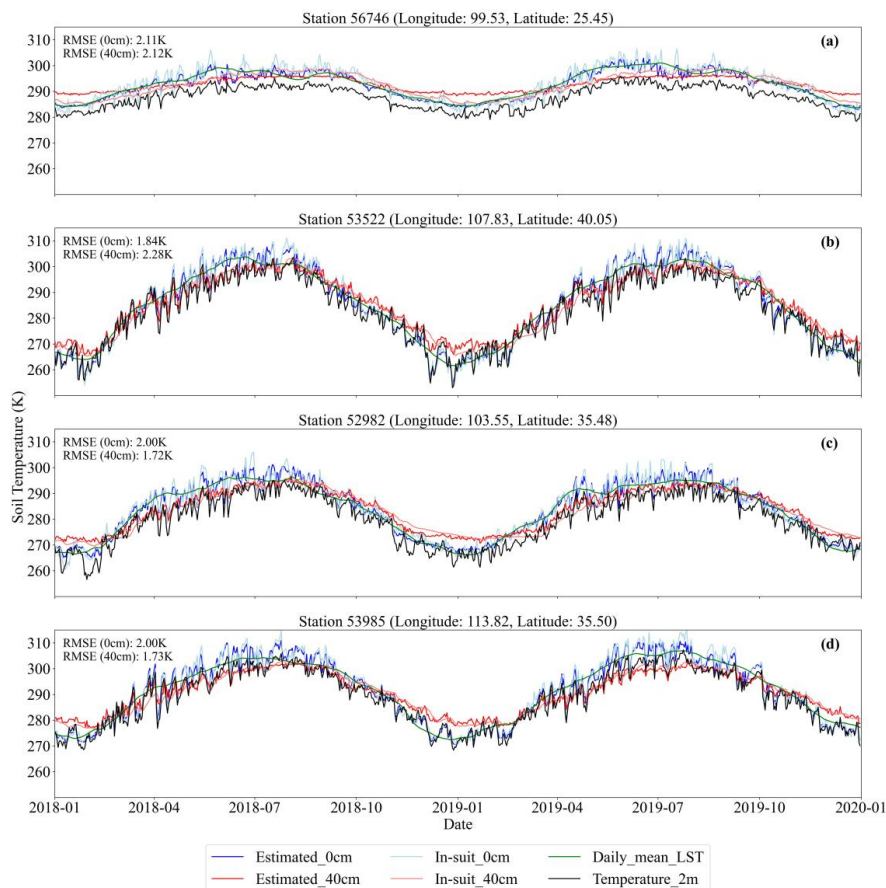


475 **Figure 11.** Spatial patterns and histograms of Estimated T_s at different depths (0, 5, 10, 15, 20, and 40 cm)

To further assess the temporal performance of T_s estimation, Fig. 12 presents the time series of estimated T_s alongside in-situ measurements at four randomly selected stations (e.g., Station 56746, 99.53°E, 25.45°N) from January 2018 to January 2020. The figure displays T_s at two depths (0 cm and 40 cm), including estimated T_s (Estimated_0cm, Estimated_40cm), in-situ T_s (In-situ_0cm, In-situ_40cm), daily mean land surface temperature (Daily_mean_LST), and 2-meter air temperature (Temperature_2m). The air temperature shows distinct seasonal cycles, while T_s



exhibits smoother temporal variations. In general, T_s reaches its peak during summer
485 and its minimum in winter, though its temporal dynamics vary with soil depth.
Specifically, T_s at 0 cm responds rapidly to air temperature changes and exhibits larger
amplitude variations, while T_s at 40 cm shows slower responses and a noticeable lag,
reflecting the damping effect of vertical heat conduction. The RMSE was used to assess
model accuracy, with RMSE values ranging from 1.72 K to 2.28 K for 0 cm and 40 cm
490 depths, indicating high consistency between estimated and observed values. Notably,
RMSE at the surface (0 cm) is slightly lower than at 40 cm, possibly due to stronger
direct influences from surface cover and meteorological conditions. Overall, the time
series analysis confirms the robustness and reliability of the model in estimating T_s
across varying depths, offering valuable insights into regional soil thermal dynamics.



495

Figure 12. Time series of the Estimated_0cm, Estimated_40cm, Daily_mean_LST,



and Temperature_2m at four sites from different regions between 2018-2019.

4. Discussion

500 4.1 The advantages of the spatially adaptive model

Previous studies have explored various approaches for constructing T_s datasets. For example, Lembrechts et al., (2022) constructed the Global Soil Bioclimatic Variables dataset using Random Forest models, based on time series data from 8,519 unique temperature sensors distributed across major terrestrial biomes worldwide. However, this dataset only provides long-term climatological averages. Subsequently, Wang et al., (2023) created a daily multi-layer T_s dataset for China (1980-2010) at 0.25° resolution, employing interpolation techniques including the thin-plate spline and the angular distance weight interpolation methods with over 2,000 in-situ observations. However, these methods do not capture the complex nonlinear relationships between T_s and factors such as meteorology, topography, and vegetation, and its coarse spatial resolution limits detailed modeling of T_s correlations.

Reanalysis datasets, which synergize data assimilation systems with numerical weather prediction and land surface modeling frameworks, provide valuable representations of land-atmosphere interactions and subsurface heat transfer processes. These products are particularly advantageous for large-scale climate simulations and long-term environmental assessments. Yang and Zhang (2018) assessed the T_s accuracy of four reanalysis datasets (ERA-Interim/Land, MERRA-2, CFSR, and GLDAS-2.0) in China using in-situ monthly mean T_s observations. The results showed that all reanalysis datasets consistently underestimated T_s across the country. More recently, the ERA5-Land and GLDAS 2.1 T_s dataset offers high temporal resolution (hourly/3-hour), but it is limited by a spatial resolution of 0.1 or 0.25 degrees. The methodological advances presented in this study address these dual challenges of accuracy and resolution. As quantified in Fig. S3, our integrated approach achieves substantial improvements in T_s estimation. Furthermore, the enhanced spatial resolution enables explicit resolution of local-scale thermal patterns that critically influence vegetation dynamics and soil biogeochemical processes.



Spatially adaptive modeling demonstrates superior adaptability and flexibility compared to traditional interpolation techniques and globally trained ML models in estimating surface T_s . A key strength of spatially adaptive approaches lies in their capacity for localized modeling, which accounts for regional variability in terrain, soil texture, and climate conditions. As illustrated in Fig. S4, the rotated quadtree method partitions spatial grids at six different orientations, enabling it to effectively capture local spatial heterogeneity. By averaging model outputs across these rotated partitions, the approach mitigates edge effects commonly associated with static grid boundaries, resulting in smoother and more continuous spatial representations. Additionally, we examined the influence of incorporating satellite-derived LST on the model's spatial accuracy. Figure. S5 demonstrates that LST is more effective than air temperature in detecting spatial variations in surface T_s in sparsely vegetated areas, with particularly notable improvements observed in northwestern China. This underscores the value of integrating multi-source remote sensing data, which significantly enhances the performance of spatially adaptive models, especially in areas characterized by low vegetation cover.

4.2 Potential applications of the T_s product

The high-resolution, multi-layer T_s datasets generated using the spatially adaptive estimation method fill a significant data gap in China, where comprehensive T_s profile records are scarce. As a key biophysical variable, T_s provides crucial insights into soil–atmosphere interactions that are not captured by air temperature alone. In agricultural systems, T_s governs fundamental processes throughout the crop life cycle—from sowing and germination to growth and yield formation (ur Rahman et al., 2019). Multi-layer T_s data can optimize accumulated temperature models, enhancing the precision of sowing decisions and supporting sustainable field management. Additionally, T_s influences nutrient decomposition and water movement within soil profiles (Jebamalar et al., 2012), directly impacting soil fertility, moisture retention, and thus, the overall efficiency of agroecosystems.



Beyond agricultural applications, T_s is increasingly recognized as a critical variable for assessing ecosystem responses to climate extremes. For instance, Fan et al., (2024) proposed the Soil Composite Drought Heatwave (SCDHW) index to evaluate the severity of concurrent drought and heatwave events. However, their findings show that existing reanalysis datasets often underestimate these events compared to observational records, highlighting the need for more accurate, high-resolution T_s data. In the context of intensifying global warming and extreme climate events, access to reliable T_s datasets is essential for improving the monitoring and prediction of environmental stressors. These advancements are not only vital for understanding terrestrial ecosystem dynamics but also for strengthening climate resilience at both regional and national scales.

Moreover, T_s plays a pivotal role in ecological and hydrological modeling, offering a more direct representation of surface processes than air temperature. It serves as a sensitive indicator of biogeochemical cycles and phenological changes (Lembrechts et al., 2022). For example, Liu et al., (2024) demonstrated that T_s is a dominant driver of spring phenology in Chinese forests, making it a valuable input for climate–vegetation interaction models. In cold regions, T_s governs soil freeze–thaw cycles, which are critical for hydrological processes such as runoff generation, groundwater recharge, and permafrost monitoring (Smith et al., 2022; Xu et al., 2022). Furthermore, T_s is a key driver of soil respiration, influencing CO₂ fluxes and terrestrial carbon cycling (Lloyd and Taylor, 1994; Hursh et al., 2017). As such, the development of high-resolution T_s products enables more accurate simulation of ecosystem carbon dynamics and regional carbon budgeting, thereby advancing our understanding of climate feedback mechanisms.

580

4.3 Limitations and future perspective

Despite the promising performance of our spatially adaptive T_s estimation framework, several limitations should be acknowledged. As illustrated in Fig. 7, stations with relatively low estimation accuracy are primarily located in southwestern



585 China. One key factor is the reliance on MODIS data from polar-orbiting satellites,
which have low temporal resolution (1–16 days) and provide instantaneous snapshots
rather than continuous observations. Although we employed a spatiotemporal linear
interpolation method to reconstruct missing data caused by cloud contamination,
residual uncertainties remain inevitable. In high-altitude regions such as the QTP and
590 the YGP, complex topography and rapidly changing climatic conditions further
exacerbate the difficulty of accurate T_s prediction, consistent with findings reported by
Mo et al., (2025).

Seasonal dynamics and land cover types also introduce considerable variability in
estimation performance. The model generally performs better in spring and autumn,
595 while summer and winter present greater challenges. During summer, dense vegetation
growth and canopy closure reduce the influence of surface–atmosphere energy
exchanges on T_s , weakening the correlation between canopy temperature and
subsurface soil temperature (Kropp et al., 2020; Cui et al., 2022). In winter, snow cover
introduces a suite of confounding effects: high surface albedo reduces net radiation
600 (Loranty et al., 2014; Li et al., 2018), while snow acts as an insulator, limiting the soil's
response to cold air incursions (Zhang, 2005; Myers-Smith et al., 2015). Additionally,
low temperatures lead to soil water freezing, altering thermal conductivity and heat
capacity. These changes, along with repeated freeze–thaw cycles, introduce significant
nonlinearity and temporal variability in T_s , ultimately reducing model accuracy (Li et
605 al., 2023; Imanian et al., 2024).

Future studies could address these limitations by incorporating data from
microwave satellite sensors, which offer all-weather imaging capabilities and can
reduce information loss caused by cloud cover in optical sensors like MODIS (Prigent
et al., 2016). Moreover, leveraging data from next-generation geostationary satellites
610 (e.g., Himawari-8), which provide observations at 10-minute intervals, may
significantly enhance temporal continuity and quality (Yamamoto et al., 2022; You et
al., 2024). Combining high-frequency geostationary data with traditional optical
sources holds great potential for advancing T_s monitoring. While our multi-source data-



driven ML model has shown strong predictive capability across multiple depths, current
615 variable importance analyses lack a mechanistic explanation for vertical heat
conduction processes. Future research could explore deep learning models that are
capable of learning complex spatiotemporal features and improving the physical
interpretability of T_s variations across time, space, and depth.

620 5. Conclusion

This study addresses the lack of high spatiotemporal resolution multi-layer T_s data
by proposing a spatially adaptive ML framework, successfully constructing a retrieval
model for multi-layer T_s . By integrating in-situ observations, reanalysis data, satellite
remote sensing data, as well as topographic and soil texture data, the model
625 demonstrates high accuracy across different depths, seasons, and land use types.
Independent validation results indicate that the model performs better in springs and
autumns compared to summers and winters, and shows superior performance in bare
land, cropland, and grassland compared to forest. Compared to ERA5_Land and
GLDAS 2.1 T_s , the multi-layer T_s data generated in this study exhibits significant
630 advantages in both accuracy and spatial detail. Based on this model, we have first
developed the long-term (2010-2020) high spatiotemporal resolution (daily, 1 km
resolution) multi-layer (0, 5, 10, 15, 20, 40 cm) T_s dataset for China. Future research
could further explore methods that simultaneously integrate temporal, spatial, and depth
information, and utilize multi-source sensor data to enhance the spatiotemporal
635 monitoring capabilities of T_s at different depths. Overall, this study demonstrates the
potential of multi-source data in T_s estimation and provides a reliable tool and data
foundation for ecological modeling, agricultural production and related studies.

6. Data availability

640 The daily multi-layer T_s products (0, 5, 10, 15, 20, and 40 cm) at 1 km resolution
from 2010 to 2020 are freely available in HDF5 format to the public at
<https://doi.org/10.11888/Terre.tpdc.302333> (Wang et al., 2025). In addition, monthly



multi-layer T_s data are also provided to meet the needs of various users.

645 **Author contributions.** XW, JM and HS developed the methodology and designed the experiments. LH and XW collected and processed the data. XW wrote the first draft of the paper under the supervision of other authors. All authors participated in the review and editing of the paper.

650 **Competing interests.** Author Hao Shi is a member of the editorial board of Earth System Science Data. The contact author has declared that no other competing interests are present.

Acknowledgments. We gratefully acknowledge the National Meteorological Center of
655 the China Meteorological Administration for providing the observed T_s data. We thank the NASA Earth Observing System Data and Information System for providing MODIS and DEM data, and the European Centre for Medium-Range Weather Forecasts for the ERA5-Land reanalysis dataset. We also acknowledge the Soil SubCenter of the National Earth System Science Data Center, National Science & Technology
660 Infrastructure of China (<http://soil.geodata.cn>), for providing soil texture data.

Financial support. This work was supported by the National Key Research and Development Program of China (Grant No. 2023YFF1303700) and the National Natural Science Foundation of China (No. 42375195).

665

Reference

- Akinwande, M.O., Dikko, H.G., Samson, A., others, 2015. Variance inflation factor: As a condition for the inclusion of suppressor variable (s) in regression analysis. *Open journal of statistics* 5, 754.
- 670 Badache, M., Eslami-Nejad, P., Ouzzane, M., Aidoun, Z., Lamarche, L., 2016. A new modeling approach for improved ground temperature profile determination. *Renewable Energy* 85, 436–444. <https://doi.org/10.1016/j.renene.2015.06.020>
- Bayatvarkeshi, M., Bhagat, S.K., Mohammadi, K., Kisi, O., Farahani, M., Hasani, A., Deo, R., Yaseen, Z.M., 2021. Modeling soil temperature using air temperature



- 675 features in diverse climatic conditions with complementary machine learning
models. *Computers and Electronics in Agriculture* 185, 106158.
- Bond-Lamberty, B., Wang, C., Gower, S.T., 2005. Spatiotemporal measurement and
modeling of stand-level boreal forest soil temperatures. *Agricultural and Forest
Meteorology* 131, 27–40. <https://doi.org/10.1016/j.agrformet.2005.04.008>
- 680 Bright, R.M., Davin, E., O'Halloran, T., Pongratz, J., Zhao, K., Cescatti, A., 2017. Local
temperature response to land cover and management change driven by non-
radiative processes. *Nature Climate Change* 7, 296–302.
- Cao, R., Chen, Y., Shen, M., Chen, J., Zhou, J., Wang, C., Yang, W., 2018. A simple
method to improve the quality of NDVI time-series data by integrating
685 spatiotemporal information with the Savitzky-Golay filter. *Remote Sensing of
Environment* 217, 244–257. <https://doi.org/10.1016/j.rse.2018.08.022>
- Chen, L., Aalto, J., Luoto, M., 2021. Observed Decrease in Soil and Atmosphere
Temperature Coupling in Recent Decades Over Northern Eurasia. *Geophysical
Research Letters* 48, e2021GL092500. <https://doi.org/10.1029/2021GL092500>
- 690 Chen, T., Guestrin, C., 2016. XGBoost: A Scalable Tree Boosting System, in:
*Proceedings of the 22nd ACM SIGKDD International Conference on
Knowledge Discovery and Data Mining, KDD '16*. Association for Computing
Machinery, New York, NY, USA, pp. 785–794.
<https://doi.org/10.1145/2939672.2939785>
- 695 Chen, X., Long, D., Hong, Y., Zeng, C., Yan, D., 2017. Improved modeling of snow and
glacier melting by a progressive two-stage calibration strategy with GRACE
and multisource data: How snow and glacier meltwater contributes to the runoff
of the U pper B rahmaputra R iver basin? *Water Resources Research* 53, 2431–
2466. <https://doi.org/10.1002/2016WR019656>
- 700 Chen, Y., Cao, R., Chen, J., Liu, L., Matsushita, B., 2021. A practical approach to
reconstruct high-quality Landsat NDVI time-series data by gap filling and the
Savitzky–Golay filter. *ISPRS Journal of Photogrammetry and Remote Sensing*
180, 174–190. <https://doi.org/10.1016/j.isprsjprs.2021.08.015>
- Cui, X., Xu, G., He, X., Luo, D., 2022. Influences of seasonal soil moisture and
705 temperature on vegetation phenology in the Qilian Mountains. *Remote Sensing*
14, 3645. <https://doi.org/10.3390/rs14153645>
- Fan, X., Zhang, Y., Shi, K., Peng, J., Liu, Yongwei, Zhou, Y., Liu, Yuanbo, Zhu, Q.,
Song, C., Wan, R., Zhao, X., Woolway, R.I., 2024. Surging compound drought–
heatwaves underrated in global soils. *Proceedings of the National Academy of
Sciences* 121, e2410294121. <https://doi.org/10.1073/pnas.2410294121>
- 710 Farhangmehr, V., Imanian, H., Mohammadian, A., Cobo, J.H., Shirkhani, H., Payeur,
P., 2025. A spatiotemporal CNN-LSTM deep learning model for predicting soil
temperature in diverse large-scale regional climates. *Science of The Total
Environment* 968, 178901. <https://doi.org/10.1016/j.scitotenv.2025.178901>
- 715 Farr, T.G., Rosen, P.A., Caro, E., Crippen, R., Duren, R., Hensley, S., Kobrick, M.,
Paller, M., Rodriguez, E., Roth, L., Seal, D., Shaffer, S., Shimada, J., Umland,
J., Werner, M., Oskin, M., Burbank, D., Alsdorf, D., 2007. The Shuttle Radar
Topography Mission. *Reviews of Geophysics* 45.



- <https://doi.org/10.1029/2005RG000183>
- 720 Feng, Y., Cui, N., Hao, W., Gao, L., Gong, D., 2019. Estimation of soil temperature from meteorological data using different machine learning models. *Geoderma* 338, 67–77. <https://doi.org/10.1016/j.geoderma.2018.11.044>
- Gao, Z., Lenschow, D.H., Horton, R., Zhou, M., Wang, L., Wen, J., 2008. Comparison of two soil temperature algorithms for a bare ground site on the Loess Plateau in China. *Journal of Geophysical Research: Atmospheres* 113. 725 <https://doi.org/10.1029/2008JD010285>
- Hu, G., Zhao, L., Wu, X., Li, R., Wu, T., Xie, C., Qiao, Y., Shi, J., Li, W., Cheng, G., 2016. New Fourier-series-based analytical solution to the conduction–convection equation to calculate soil temperature, determine soil thermal 730 properties, or estimate water flux. *International Journal of Heat and Mass Transfer* 95, 815–823. <https://doi.org/10.1016/j.ijheatmasstransfer.2015.11.078>
- Huang, R., Huang, J., Zhang, C., Ma, H., Zhuo, W., Chen, Y., Zhu, D., Wu, Q., Mansaray, L.R., 2020. Soil temperature estimation at different depths, using remotely-sensed data. *Journal of Integrative Agriculture* 19, 277–290. 735 [https://doi.org/10.1016/S2095-3119\(19\)62657-2](https://doi.org/10.1016/S2095-3119(19)62657-2)
- Huete, A., Didan, K., Miura, T., Rodriguez, E.P., Gao, X., Ferreira, L.G., 2002. Overview of the radiometric and biophysical performance of the MODIS vegetation indices. *Remote Sensing of Environment, The Moderate Resolution Imaging Spectroradiometer (MODIS): a new generation of Land Surface 740 Monitoring* 83, 195–213. [https://doi.org/10.1016/S0034-4257\(02\)00096-2](https://doi.org/10.1016/S0034-4257(02)00096-2)
- Hursh, A., Ballantyne, A., Cooper, L., Maneta, M., Kimball, J., Watts, J., 2017. The sensitivity of soil respiration to soil temperature, moisture, and carbon supply at the global scale. *Global Change Biology* 23, 2090–2103.
- Imanian, H., Mohammadian, A., Farhangmehr, V., Payeur, P., Goodarzi, D., Hiedra Cobo, J., Shirkhani, H., 2024. A comparative analysis of deep learning models for soil temperature prediction in cold climates. *Theoretical and Applied 745 Climatology* 155, 2571–2587. <https://doi.org/10.1007/s00704-023-04781-x>
- Jebamalar, A.S., Raja, S., Bai, S., 2012. Prediction of annual and seasonal soil temperature variation using artificial neural network. 92.40. *Lg*; 84.35.+ i.
- 750 Karthikeyan, L., Mishra, A.K., 2021. Multi-layer high-resolution soil moisture estimation using machine learning over the United States. *Remote Sensing of Environment* 266, 112706. <https://doi.org/10.1016/j.rse.2021.112706>
- Khosravi, K., Golkarian, A., Barzegar, R., Aalami, M.T., Heddami, S., Omidvar, E., Keesstra, S.D., López-vicente, M., 2023. Multi-step ahead soil temperature 755 forecasting at different depths based on meteorological data: Integrating resampling algorithms and machine learning models. *Pedosphere* 33, 479–495. <https://doi.org/10.1016/j.pedsph.2022.06.056>
- Kong, D., Zhang, Y., Gu, X., Wang, D., 2019. A robust method for reconstructing global MODIS EVI time series on the Google Earth Engine. *ISPRS Journal of 760 Photogrammetry and Remote Sensing* 155, 13–24. <https://doi.org/10.1016/j.isprsjprs.2019.06.014>
- Kropp, H., Loranty, M.M., Natali, S.M., Kholodov, A.L., Rocha, A.V., Myers-Smith, I.,



- Abbot, B.W., Abermann, J., Blanc-Betes, E., Blok, D., others, 2020. Shallow soils are warmer under trees and tall shrubs across arctic and boreal ecosystems. *Environmental research letters* 16, 015001.
- 765
- Lembrechts, J.J., van den Hoogen, J., Aalto, J., Ashcroft, M.B., 2022. Global maps of soil temperature. *Global Change Biology* 28, 3110–3144. <https://doi.org/10.1111/gcb.16060>
- Li, B., Liang, S., Ma, H., Dong, G., Liu, X., He, T., Zhang, Y., 2024. Generation of global 1 km all-weather instantaneous and daily mean land surface temperatures from MODIS data. *Earth System Science Data* 16, 3795–3819. <https://doi.org/10.5194/essd-16-3795-2024>
- 770
- Li, N., Wang, L., Chen, D., 2024. Vegetation greening amplifies shallow soil temperature warming on the Tibetan Plateau. *npj Clim Atmos Sci* 7, 1–12. <https://doi.org/10.1038/s41612-024-00651-z>
- 775
- Li, Q., Ma, M., Wu, X., Yang, H., 2018. Snow cover and vegetation-induced decrease in global albedo from 2002 to 2016. *Journal of Geophysical Research: Atmospheres* 123, 124–138.
- Li, Q., Zhu, Y., Shangguan, W., Wang, X., Li, L., Yu, F., 2022. An attention-aware LSTM model for soil moisture and soil temperature prediction. *Geoderma* 409, 115651. <https://doi.org/10.1016/j.geoderma.2021.115651>
- 780
- Li, X., Zhang, L., Wang, X., Liang, B., 2024. Forecasting greenhouse air and soil temperatures: A multi-step time series approach employing attention-based LSTM network. *Computers and Electronics in Agriculture* 217, 108602. <https://doi.org/10.1016/j.compag.2023.108602>
- 785
- Li, X., Zhu, Y., Li, Q., Zhao, H., Zhu, J., Zhang, C., 2023. Interpretable spatio-temporal modeling for soil temperature prediction. *Frontiers in Forests and Global Change* 6, 1295731. <https://doi.org/10.3389/ffgc.2023.1295731>
- Liu, F., Wu, H., Zhao, Y., Li, D., Yang, J.-L., Song, X., Shi, Z., Zhu, A.-X., Zhang, G.-L., 2022. Mapping high resolution National Soil Information Grids of China. *Science Bulletin* 67, 328–340. <https://doi.org/10.1016/j.scib.2021.10.013>
- 790
- Liu X., Li Z.-L., Duan S.-B., Leng P., Si M., 2025. Retrieval of global surface soil and vegetation temperatures based on multisource data fusion. *Remote Sensing of Environment* 318, 114564. <https://doi.org/10.1016/j.rse.2024.114564>
- 795
- Liu, Y., Liu, X., Fu, Z., Zhang, D., Liu, L., 2024. Soil temperature dominates forest spring phenology in China. *Agricultural and Forest Meteorology* 355, 110141. <https://doi.org/10.1016/j.agrformet.2024.110141>
- Lloyd, J., Taylor, J., 1994. On the temperature dependence of soil respiration. *Functional ecology* 315–323.
- 800
- Loranty, M.M., Berner, L.T., Goetz, S.J., Jin, Y., Randerson, J.T., 2014. Vegetation controls on northern high latitude snow-albedo feedback: Observations and CMIP 5 model simulations. *Global change biology* 20, 594–606.
- Mahanama, S.P.P., Koster, R.D., Reichle, R.H., Suarez, M.J., 2008. Impact of Subsurface Temperature Variability on Surface Air Temperature Variability: An AGCM Study. *Journal of Hydrometeorology* 9, 804–815. <https://doi.org/10.1175/2008JHM949.1>
- 805



- Mo, Y., Pepin, N., Lovell, H., 2025. Understanding temperature variations in mountainous regions: The relationship between satellite-derived land surface temperature and in situ near-surface air temperature. *Remote Sensing of Environment* 318, 114574.
- 810 Mortier, S., Hamedpour, A., Bussmann, B., Wandji, R.P.T., Latré, S., Sigurdsson, B.D., De Schepper, T., Verdonck, T., 2024. Inferring the relationship between soil temperature and the normalized difference vegetation index with machine learning. *Ecological Informatics* 82, 102730.
- 815 Muñoz-Sabater, J., Dutra, E., Agustí-Panareda, A., Albergel, C., Arduini, G., Balsamo, G., Boussetta, S., Choulga, M., Harrigan, S., Hersbach, H., Martens, B., Miralles, D.G., Piles, M., Rodríguez-Fernández, N.J., Zsoter, E., Buontempo, C., Thépaut, J.-N., 2021. ERA5-Land: a state-of-the-art global reanalysis dataset for land applications. *Earth System Science Data* 13, 4349–4383. <https://doi.org/10.5194/essd-13-4349-2021>
- 820 Myers-Smith, I.H., Elmendorf, S.C., Beck, P.S., Wilmking, M., Hallinger, M., Blok, D., Tape, K.D., Rayback, S.A., Macias-Fauria, M., Forbes, B.C., others, 2015. Climate sensitivity of shrub growth across the tundra biome. *Nature climate change* 5, 887–891.
- 825 Nahvi, B., Habibi, J., Mohammadi, K., Shamshirband, S., Al Razgan, O.S., 2016. Using self-adaptive evolutionary algorithm to improve the performance of an extreme learning machine for estimating soil temperature. *Computers and Electronics in Agriculture* 124, 150–160. <https://doi.org/10.1016/j.compag.2016.03.025>
- Ochsner, T.E., Horton, R., Ren, T., 2001. A new perspective on soil thermal properties. *Soil science society of America Journal* 65, 1641–1647. <https://doi.org/10.2136/sssaj2001.1641>
- 830 Prigent, C., Jimenez, C., Aires, F., 2016. Toward “all weather,” long record, and real-time land surface temperature retrievals from microwave satellite observations. *Journal of Geophysical Research: Atmospheres* 121, 5699–5717. <https://doi.org/10.1002/2015JD024402>
- 835 Shati, F., Prakash, S., Norouzi, H., Blake, R., 2018. Assessment of differences between near-surface air and soil temperatures for reliable detection of high-latitude freeze and thaw states. *Cold Regions Science and Technology* 145, 86–92. <https://doi.org/10.1016/j.coldregions.2017.10.007>
- 840 Smith, S.L., O’Neill, H.B., Isaksen, K., Noetzli, J., Romanovsky, V.E., 2022. The changing thermal state of permafrost. *Nat Rev Earth Environ* 3, 10–23. <https://doi.org/10.1038/s43017-021-00240-1>
- ur Rahman, M.H., Ahmad, A., Wajid, A., Hussain, M., Rasul, F., Ishaque, W., Islam, M.A., Shelia, V., Awais, M., Ullah, A., others, 2019. Application of CSM-CROPGRO-Cotton model for cultivars and optimum planting dates: Evaluation in changing semi-arid climate. *Field Crops Research* 238, 139–152. <https://doi.org/10.1016/j.fcr.2017.07.007>
- 845 Wan, Z., Dozier, J., 1996. A generalized split-window algorithm for retrieving land-surface temperature from space. *IEEE Transactions on geoscience and remote sensing* 34, 892–905. <https://doi.org/10.1109/36.508406>
- 850



- Wang, D., Wang, A., Wang, Z., 2023. A multilayer daily high-resolution gridded homogenized soil temperature over continental China. *International Journal of Climatology* 43, 2015–2030. <https://doi.org/10.1002/joc.7959>
- 855 Wang, K., Dickinson, R.E., 2013. Contribution of solar radiation to decadal temperature variability over land. *Proceedings of the National Academy of Sciences* 110, 14877–14882.
- Wang, X., He, L., Shi, H., Yu, Q., 2025. Daily multi-layer soil temperature dataset with 1 km resolution in China from 2010 to 2020. National Tibetan Plateau Data Center. <https://doi.org/10.11888/Terre.tpdc.302333>
- 860 Xing, L., Li, L., Gong, J., Ren, C., Liu, J., Chen, H., 2018. Daily soil temperatures predictions for various climates in United States using data-driven model. *Energy* 160, 430–440. <https://doi.org/10.1016/j.energy.2018.07.004>
- Xu, C., Liao, S., Huang, L., Xia, J., 2023. Soil temperature estimation at different depths over the central Tibetan Plateau integrating multiple Digital Earth observations and geo-computing. *International Journal of Digital Earth* 16, 4023–4043. <https://doi.org/10.1080/17538947.2023.2264267>
- 865 Xu, C., Qu, J.J., Hao, X., Zhu, Z., Gutenberg, L., 2020. Surface soil temperature seasonal variation estimation in a forested area using combined satellite observations and in-situ measurements. *International Journal of Applied Earth Observation and Geoinformation* 91, 102156.
- 870 Xu, S., Fu, Q., Li, T., Meng, F., Liu, D., Hou, R., Li, M., Li, Q., 2022. Spatiotemporal characteristics of the soil freeze-thaw state and its variation under different land use types - A case study in Northeast China. *Agricultural and Forest Meteorology* 312, 108737. <https://doi.org/10.1016/j.agrformet.2021.108737>
- 875 Yamamoto, Y., Ichii, K., Ryu, Y., Kang, M., Murayama, S., 2022. Uncertainty quantification in land surface temperature retrieved from Himawari-8/AHI data by operational algorithms. *ISPRS Journal of Photogrammetry and Remote Sensing* 191, 171–187. <https://doi.org/10.1016/j.isprsjprs.2022.07.008>
- 880 Yang, K., Zhang, J., 2018. Evaluation of reanalysis datasets against observational soil temperature data over China. *Clim Dyn* 50, 317–337. <https://doi.org/10.1007/s00382-017-3610-4>
- Yang, Q., Xu, M., Liu, H., Wang, J., Liu, L., Chi, Y., Zheng, Y., 2011. Impact factors and uncertainties of the temperature sensitivity of soil respiration. *Shengtai Xuebao/Acta Ecologica Sinica* 31, 2301–2311.
- 885 You, W., Huang, C., Hou, J., Zhang, Y., Dou, P., Han, W., 2024. Reconstruction of MODIS LST Under Cloudy Conditions by Integrating Himawari-8 and AMSR-2 Data Through Deep Forest Method. *IEEE Trans. Geosci. Remote Sensing* 62, 1–17. <https://doi.org/10.1109/TGRS.2024.3388409>
- Zhang, T., 2005. Influence of the seasonal snow cover on the ground thermal regime: An overview. *Reviews of Geophysics* 43.
- 890 Zhang, Y., Chen, W., Smith, S.L., Riseborough, D.W., Cihlar, J., 2005. Soil temperature in Canada during the twentieth century: Complex responses to atmospheric climate change. *Journal of Geophysical Research: Atmospheres* 110. <https://doi.org/10.1029/2004JD004910>



- 895 Zhao, T., Liu, S., Xu, J., He, H., Wang, D., Horton, R., Liu, G., 2022. Comparative analysis of seven machine learning algorithms and five empirical models to estimate soil thermal conductivity. *Agricultural and Forest Meteorology* 323, 109080. <https://doi.org/10.1016/j.agrformet.2022.109080>